iScience

Article

# Optimized Ag enhances antibacterial activity and corrosion resistance of extruded Mg-2Zn-0.2Ca alloy

## Graphical abstract

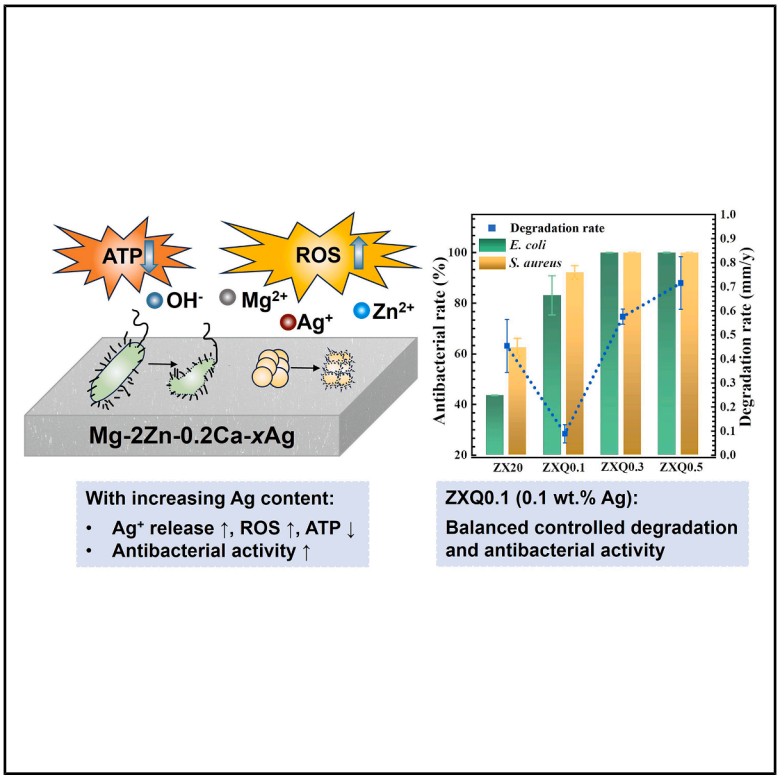


## Authors

Fang Yi, Yi Chen, Dikai Guan, Lingzhi Yang, Junjie Li, Yonghao Gao

## Correspondence

gaoyonghao_009@163.com

## In brief

Corrosion; Bioengineering; Materials science

## Highlights

- 0.1 wt % Ag addition reduces long-term degradation of Mg-2Zn-0.2Ca alloy
- Higher Ag contents accelerated degradation and antibacterial ion release
- $Ag^+$ release and pH elevation enhance ROS, ATP depletion, and antibacterial effects
- Mg-2Zn-0.2Ca-0.1Ag achieved balanced degradation and antibacterial performance

Yi et al., 2026, iScience *29*, 117220
September 18, 2026 
https://doi.org/10.1016/j.isci.2026.117220

CellPress

iScience

CellPress
OPEN ACCESS

Article

# Optimized Ag enhances antibacterial activity and corrosion resistance of extruded Mg-2Zn-0.2Ca alloy

Fang Yi,[1,5,6] Yi Chen,[2] Dikai Guan,[3] Lingzhi Yang,[4] Junjie Li,[2] and Yonghao Gao[2,7,*]
[1]Xiangya School of Stomatology, Central South University, Changsha, Hunan 410008, China
[2]School of Materials Science and Engineering, Central South University, Changsha, Hunan 410083, China
[3]Department of Mechanical Engineering, School of Engineering, University of Southampton, Southampton SO17 1BJ, UK
[4]School of Minerals Processing and Bioengineering, Central South University, Changsha, Hunan 410083, China
[5]Hunan Clinical Research Center of Oral Major Diseases and Oral Health, Changsha, Hunan 410008, China
[6]Hunan Xiangya Stomatological Hospital, Central South University, Changsha, Hunan 410008, China
[7]Lead contact
*Correspondence: gaoyonghao_009@163.com
https://doi.org/10.1016/j.isci.2026.117220

## SUMMARY

Infection remains a major cause of implant failure, motivating the development of biodegradable metals with intrinsic antibacterial activity. This study investigated how minor silver (Ag) addition regulates the degradation and antibacterial performance of extruded Mg-2Zn-0.2Ca alloys. Adding 0.1 wt % Ag significantly reduced the degradation rate to 0.14 ± 0.04 mm/y after 672 h of immersion, lower than WE43 (0.66 ± 0.05 mm/y), whereas higher Ag contents accelerated degradation. Extracts from the Ag-free alloy showed moderate antibacterial rates of 43.4% ± 0.06% and 62.4% ± 3.55% against *Escherichia coli* and *Staphylococcus aureus*, respectively. With 0.1 wt % Ag, these rates increased significantly to 83.4% ± 3.82% and 92.1% ± 2.66%, comparable to WE43. Adenosine triphosphate assays, reactive oxygen species detection, and electron paramagnetic resonance analysis indicated that the enhanced antibacterial activity of Ag-containing alloys involved adenosine triphosphate depletion and oxidative stress. Overall, ZXQ0.1 represents a promising candidate for further investigation as a biodegradable antimicrobial magnesium alloy.

## INTRODUCTION

Implant-associated infection (IAI) remains one of the most challenging postoperative complications, with reported incidence rates as high as 15%–55%,[1] severely compromising surgical outcomes and functional recovery. Clinically, infection can lead to devastating consequences, including malunion, nonunion, osteomyelitis, sepsis, amputation, and even death.[2] Current management relies on surgical debridement and systemic antibiotics, which often fail due to insufficient local concentrations and biofilm-mediated resistance, while prolonged use increases the risk of antibiotic-resistant strains.[3] Various anti-infective strategies have been developed, including antibiotic coatings, antibacterial metal ion incorporation,[4] and photo-responsive polymer coatings.[5] However, infection risk persists throughout the implant's service life, making IAI a continuing clinical challenge.

Biodegradable implants with intrinsic antibacterial functionality have emerged as an alternative to temporary orthopedic materials. Magnesium (Mg) alloys are considered promising biodegradable metallic implant candidates due to their favorable biocompatibility, bioactivity, biodegradability, and an elastic modulus close to that of natural bone.[6,7] However, rapid degradation and localized corrosion under physiological environments may lead to gas accumulation and premature mechanical failure, limiting clinical use. Alloying has been widely employed to optimize the comprehensive performance of Mg-based materials.[8] In recent years, biodegradable antibacterial Mg alloys containing Ag, Zn, Cu, Ga, and other antibacterial elements have attracted increasing attention for their potential to integrate biodegradability, mechanical support, and infection resistance.[9–12] However, achieving sustained antibacterial activity while maintaining controlled degradation remains a central challenge. Mg-Zn-Ca system, particularly Mg-2Zn-0.2Ca, shows a balanced combination of mechanical strength, corrosion resistance, and biocompatibility,[13–15] highlighting its potential for orthopedic applications.[16]

Although Mg can exhibit antibacterial effects under certain conditions, enhancement is generally required to meet clinical demands. Introducing antibacterial elements into Mg-based alloys via alloying is an effective approach to strengthen antibacterial performance.[17,18] Compared with antibiotics, metal ions typically provide broad-spectrum antibacterial activity and are less prone to inducing bacterial resistance. Silver (Ag) is a well-known broad-spectrum antibacterial agent and has been incorporated into Mg alloys to enhance antibacterial performance

while modulating microstructure, mechanical properties, and degradation behavior.[19–21] However, because Ag incorporation can modify phase constitution and intensify micro-galvanic interactions, its influence on alloy degradation requires careful optimization.

A key challenge is therefore achieving effective antibacterial activity while maintaining controllable degradation. The reported effects of Ag on Mg alloy biodegradation are inconsistent: some studies indicate reduced corrosion resistance,[12,20] whereas others report improvements.[22,23] Chen et al.[24] introduced 1.5 and 2.5 wt % Ag into Mg-0.8Ca-5Zn alloys and observed enhanced corrosion resistance and good *in vitro* biocompatibility. Ma et al.[25] reported that Mg-1Zn-0.2Ca-1Ag exhibited the lowest degradation rate, whereas higher Ag content (>1 wt %) accelerated degradation. Another study found that 0.3 wt % Ag in Mg-3Zn-0.2Ca improved mechanical and degradation performance without cytotoxicity.[22] These discrepancies highlight the need for systematic investigations correlating Ag content, degradation behavior, and antibacterial performance under physiologically relevant conditions.

Small Ag additions (<0.5 wt %) refine precipitate distribution and slightly improve hardness and strength[22,26]; very low Ag (<0.1 wt %) may be insufficient for antibacterial efficacy, whereas higher Ag (>0.5 wt %) may cause Ag enrichment in secondary phases, promoting micro-galvanic corrosion.[12,27,28] To address these gaps, extruded Mg-2Zn-0.2Ca-*x*Ag alloys ($x$ = 0, 0.1, 0.3, and 0.5 wt %) were investigated. Ag was incorporated as a microalloying element to enhance antibacterial performance while moderately tuning mechanical and degradation properties. Our prior work demonstrated that these extruded Mg-2Zn-0.2Ca-*x*Ag alloys meet the mechanical requirements for implant applications (UTS > 200 MPa and FE > 10%),[29] and their microstructure, mechanical degradation, and short-term degradation behavior in Hank's solution were characterized.[30] However, the long-term degradation behavior, ion release profile, antibacterial response, and potential antibacterial mechanism of low-Ag Mg-2Zn-0.2Ca alloys remain insufficiently understood. In the present study, we further evaluate long-term *in vitro* degradation for up to 672 h and multidimensional antibacterial performance, including bacterial viability, intracellular adenosine triphosphate (ATP) levels, and reactive oxygen species (ROS) generation, to elucidate how minor Ag addition balances corrosion resistance and antibacterial efficacy, thereby providing guidance for the design of biodegradable Mg alloys. Our results showed that 0.1 wt % Ag achieved the optimal balance between controlled degradation and antibacterial activity, thereby identifying ZXQ0.1 as a promising biodegradable antimicrobial Mg alloy candidate for further biomedical investigation and providing guidance for the design of Ag-containing biodegradable Mg alloys.

## RESULTS

### *In vitro* degradation evaluation

The *in vitro* degradation behavior of the as-extruded Mg-2Zn-0.2Ca-*x*Ag alloys in Hank's solution is summarized in Figure 1. ZXQ0.1(Mg-2Zn-0.2Ca-0.1Ag) showed the lowest mass loss (1.11% ± 0.37%), which was significantly lower than that of ZX20, ZXQ0.3, ZXQ0.5, and WE43 (Figure 1A). Consistently, ZXQ0.1 exhibited the lowest degradation rate, indicating that minor Ag incorporation effectively enhanced corrosion resistance. In contrast, further increasing the Ag content to 0.3 wt % and 0.5 wt % led to a marked increase in degradation rate compared with ZXQ0.1, suggesting compromised corrosion resistance. After 672 h of immersion, ZXQ0.5 exhibited the highest degradation rate (0.70 ± 0.07 mm/y), approximately five times higher than that of ZXQ0.1 (Figure 1B). These results indicate a non-linear, Ag-composition-dependent effect on the degradation behavior of Mg-2Zn-0.2Ca alloys, whereby 0.1 wt % Ag improves corrosion resistance and higher Ag contents (0.3–0.5 wt %) accelerates degradation.

The evolution of $Mg^{2+}$ concentration in Hank's solution (Figure 1C) exhibited trends consistent with the mass loss results. The initial $Mg^{2+}$ concentration was 23.0 ± 0.3 mg/L and gradually increased with immersion time. During the first 336 h, the increase in $Mg^{2+}$ concentration was relatively moderate, which can be attributed to the formation of corrosion product layers on the alloy surface that partially impeded further $Mg^{2+}$ release. Beyond 336 h, the $Mg^{2+}$ concentration increased more rapidly, suggesting localized rupture or detachment of the corrosion product layer, leading to accelerated degradation. After 672 h, the $Mg^{2+}$ concentrations released from ZX20 and ZXQ0.1 climbed to 376.8 ± 15.5 mg/L and 281.6 ± 19.4 mg/L, respectively, both below the reported tolerance limit for $Mg^{2+}$ in the human body.[31] In contrast, ZXQ0.3 and ZXQ0.5 released substantially higher $Mg^{2+}$ concentrations, indicating more pronounced degradation behavior. The pH evolution of the immersion solutions further corroborated these trends (Figure 1D). The pH variation could be divided into three stages: a rapid increase during the initial stage (0–168 h), corresponding to intense alloy dissolution; a plateau stage (168–336 h), suggesting partial inhibition of degradation; and a slight decrease during the later stage (336–672 h), likely due to the consumption of $OH^-$ by corrosion products. Throughout the immersion period, the pH values of ZX20 and ZXQ0.1 remained consistently lower than those of the higher-Ag alloys, with ZXQ0.1 exhibiting the lowest pH value after 672 h (9.66 ± 0.29), further confirming its improved corrosion resistance. Scanning electron microscopy (SEM) observations after 3 h of immersion revealed early-stage degradation characterized by filiform corrosion and pitting in all alloy groups (Figure S1), with pits preferentially initiating near second-phase particles or second phase/matrix interfaces. After 672 h, 3D laser profilometry confirmed composition-dependent localized degradation (Figure S2): ZXQ0.1 showed moderate corrosion depth comparable to ZX20, whereas ZXQ0.3 and ZXQ0.5 exhibited deeper pits and larger corroded areas, consistent with their higher degradation rates.

### pH and ion concentration of alloy extracts

Figure 2 summarizes the concentrations of $Mg^{2+}$, $Zn^{2+}$, and $Ag^{+}$, together with the pH values of extracts obtained from the as-extruded Mg-2Zn-0.2Ca-*x*Ag alloys ($x$ = 0, 0.1, 0.3, and 0.5 wt %) and WE43 alloy after 72 h of immersion in Hank's solution. The $Ca^{2+}$ concentration showed no noticeable differences among groups and is therefore not

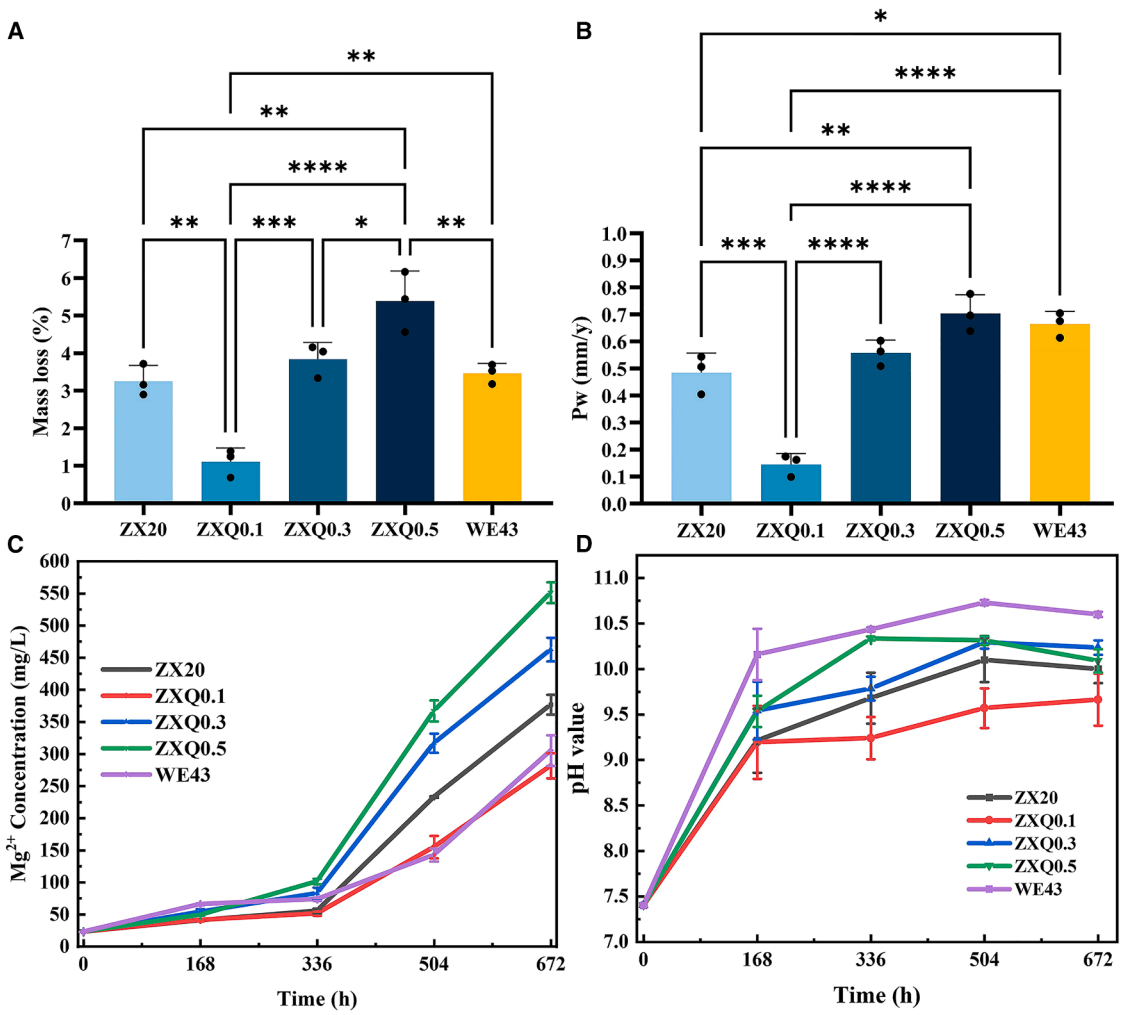


**Figure 1. *In vitro* degradation behavior of as-extruded Mg-2Zn-0.2Ca-*x*Ag alloys after 672 h of immersion in Hank's solution**

(A) Mass loss.

(B) Degradation rate.

(C) $Mg^{2+}$ concentration as a function of immersion time.

(D) pH variation as a function of immersion time.

Data are presented as mean ± SD ($n$ = 3 independent alloy samples per group). *$p$ < 0.05, **$p$ < 0.01, ***$p$ < 0.001, ****$p$ < 0.0001.

presented. These ion concentrations were used to characterize the extract environment for subsequent antibacterial evaluation. As shown in Figure 2A, the $Mg^{2+}$ concentration in the extract of ZXQ0.1 (88.7 ± 7.8 mg/L) was slightly higher than that in ZX20 (78.5 ± 1.0 mg/L). In contrast, further increasing the Ag content to 0.3 wt % and 0.5 wt % resulted in a significant elevation of $Mg^{2+}$ concentration compared with ZXQ0.1, supporting that excessive Ag addition accelerates Mg matrix degradation. Among all tested materials, the WE43 alloy released the highest $Mg^{2+}$ concentration, suggesting its more pronounced degradation. Unlike $Mg^{2+}$ release, $Zn^{2+}$ release showed no clear dependence on Ag content in the alloy (Figure 2B), which can be attributed to the inherently low Zn fraction within the designed alloy system. By comparison, the concentration of released $Ag^{+}$ is governed jointly by the alloy degradation kinetics and the nominal Ag in the bulk alloy. As displayed in Figure 2C, $Ag^{+}$ was only measurable in the Ag-alloyed samples, reaching 7.4 ± 0.5 μg/L for ZXQ0.1 and rising to 23.2 ± 1.6 μg/L for ZXQ0.5. Considering the well-reported antibacterial effect of $Ag^{+}$, the alloy with higher Ag addition may have better antibacterial performance. The pH values of the alloy extracts are shown in Figure 2D. All extracts exhibited alkaline pH values. Compared with the Ag-free alloy, the pH changed only slightly after the addition of 0.1 wt % Ag but increased significantly at higher Ag contents, consistent with the $Mg^{2+}$ release profile. The extract from WE43 showed the highest pH, indicating more pronounced alkalization of the extraction medium. These results suggest that ZXQ0.1 achieved a balanced degradation and ion-release behavior.

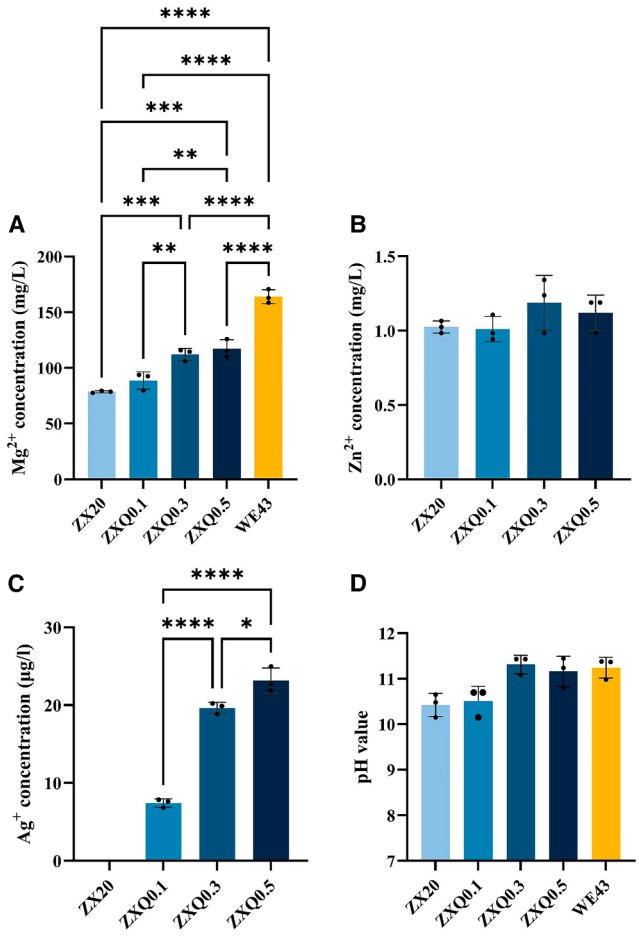


**Figure 2. Ion concentrations and pH values of extracts from as-extruded Mg-2Zn-0.2Ca-*x*Ag alloys**

(A) $Mg^{2+}$ concentration.

(B) $Zn^{2+}$ concentration.

(C) $Ag^{+}$ concentration.

(D) pH values.

Data are presented as mean ± SD ($n = 3$ independent alloy extract preparations per group). *$p < 0.05$, **$p < 0.01$, ***$p < 0.001$, ****$p < 0.0001$.

## Antibacterial activity of Mg-2Zn-0.2Ca-xAg alloys

### *Bacterial adhesion behavior*

The bacterial adhesion behavior on Mg-2Zn-0.2Ca-*x*Ag alloys was evaluated by SEM after direct co-culture with *E. coli* and *S. aureus*. Representative SEM images of *E. coli* and *S. aureus* adhered to alloy surfaces after 4 h are shown in Figure 3. On the Ti-6Al-4V control surface, *E. coli* cells exhibited intact rod-like morphology (approximately 1–2 μm in length and approximately 0.5 μm in width), indicating normal bacterial adhesion and viability. In contrast, bacteria on the surfaces of Mg-2Zn-0.2Ca-*x*Ag alloys displayed pronounced morphological abnormalities, including shortened and wrinkled rod-like shapes, cellular collapse, and severe membrane damage (as indicated by the yellow arrows in Figure 3). Notably, dumbbell-like morphology was observed on the ZXQ0.3 and WE43 surfaces, whereas extensive membrane rupture was evident on the ZXQ0.5. For *S. aureus*, cells on Ti-6Al-4V maintained typical spherical or ellipsoidal morphology (approximately 0.5–1 μm in diameter) and formed dense grape-like clusters with smooth and intact surfaces. In contrast, significantly fewer bacteria adhered to Mg-2Zn-0.2Ca-*x*Ag alloy surfaces, and the cells displayed disrupted cell walls, collapsed spherical structures, surface indentations, and dispersed clusters. Overall, these observations demonstrate that Ag-containing alloys inhibit bacterial adhesion and induce severe morphological damage to both Gram-negative and Gram-positive bacteria. After 8 h of co-culture, bacteria adhere to the Ti-6Al-4V alloy, whereas hardly any bacteria can be observed on the Mg surfaces (Figure S3). SEM images of bacteria exposed to alloy extracts further showed membrane disruption, cellular collapse, and loss of structural integrity (Figure S4). These results further confirm that Mg-2Zn-0.2Ca-*x*Ag alloys suppress bacterial adhesion and damage bacterial morphology through both direct-contact and extract-mediated effects.

### *Antibacterial efficiency*

Bacterial cultures were incubated with alloy extracts for 24 h to evaluate extract-mediated antibacterial activity (Figure 4). Compared with the negative control, all Mg alloy extracts significantly reduced bacterial colony numbers, and Ag-containing alloys exhibited a markedly enhanced antibacterial effect. The antibacterial rates of the extracts are quantified in Figure 5. For *E. coli*, the Ag-free Mg-2Zn-0.2Ca (ZX20) extract exhibited a relatively low antibacterial rate (43.4% ± 0.06%). The addition of 0.1 wt % Ag significantly increased the antibacterial rate to 83.4% ± 3.82%, nearly doubling the antibacterial efficacy. Further Ag additions (0.3 and 0.5 wt %) resulted in antibacterial rates exceeding 99%. Overall, the antibacterial performance against *E. coli* followed the order: ZX20 < ZXQ0.1 < WE43 < ZXQ0.3 < ZXQ0.5. A similar trend was observed for *S. aureus* (Figure 5B). The antibacterial rate increased significantly from 62.4% ± 3.55% for the Ag-free alloy to 92.1% ± 2.66% after adding 0.1 wt % Ag, while further Ag addition yielded antibacterial rates above 99.9%. The antibacterial efficacy followed the order: ZX20 < WE43 < ZXQ0.1 < ZXQ0.3 < ZXQ0.5, indicating an Ag-content-dependent enhancement of extract-mediated antibacterial activity. Spearman correlation analysis further showed a positive association between $Ag^{+}$ concentration and the *E. coli* antibacterial rate (Figure S7A), supporting a quantitative link between $Ag^{+}$ release and enhanced antibacterial efficacy. Ultrasonic elution followed by plate counting and 24 h direct co-culture assays further confirmed the anti-adhesion and direct-contact antibacterial performance of the alloys (Figures S5 and S6). Together with the degradation results (Figure 1), these findings indicate a trade-off between antibacterial efficacy and degradation stability. Higher Ag contents enhanced antibacterial activity, likely through increased $Ag^{+}$ release, but also accelerated degradation, highlighting the need to balance antibacterial performance with controlled degradation.

### *Effects on bacterial viability and metabolic activity*

Live/dead fluorescence staining was employed to assess bacterial viability after exposure to alloy extracts for 24 h. As shown in Figure 6A, *E. coli* treated with Mg-2Zn-0.2Ca-*x*Ag extracts exhibited predominantly red fluorescence, indicating dead bacteria, whereas the control group displayed mainly green

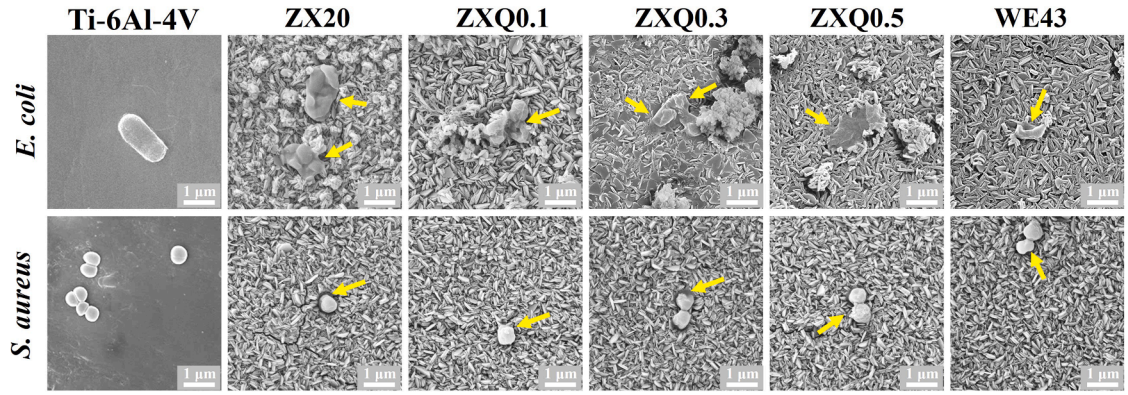


**Figure 3. Bacterial adhesion morphology of *E. coli* and *S. aureus* after direct co-culture with as-extruded Mg-2Zn-0.2Ca-*x*Ag alloys for 4 h**
Representative SEM images from a single experiment are shown, with multiple randomly selected fields examined for each sample. Scale bars: 1 μm.

fluorescence, indicating viable bacteria. Quantitative analysis (Figure 6B) revealed a significantly higher proportion of dead bacteria in all Mg alloy extract groups compared with the control. Ag-containing extracts induced a higher level of bacterial death than the Ag-free alloy and WE43, although the differences were not statistically significant. Similar results were observed for *S. aureus* (Figure 6C). Exposure to Mg-2Zn-0.2Ca-*x*Ag extracts resulted in extensive bacterial death, with significantly higher dead cell counts than the control. Ag addition further increased bacterial mortality, but no statistically significant differences were observed among the Ag-containing groups.

Bacterial metabolic activity was further evaluated by ATP quantification (Figure 7). The ATP levels of *E. coli* decreased markedly after co-culture with alloy extracts, following the order: control > ZX20 > ZXQ0.1 > ZXQ0.3 > ZXQ0.5. Spearman correlation analysis further showed that ATP levels were negatively associated with the *E. coli* antibacterial rate (Figure S7B), supporting a quantitative link between ATP depletion and enhanced antibacterial activity. These results suggest that alloy extracts impaired bacterial energy metabolism and/or induced extensive bacterial death, consistent with the increased $Ag^{+}$ release and improved antibacterial performance.

### *ROS-related antibacterial mechanism*

Under normal conditions, ROS generated by cellular metabolism are maintained in a dynamic balance with the antioxidant system. When this balance is disrupted, excessive ROS accumulation can damage bacterial proteins, DNA, and lipids, thereby interfering with their metabolism and proliferation, ultimately leading to bacterial cell death.[32,33] To investigate the potential involvement of oxidative stress in antibacterial activity, intracellular ROS generation was evaluated, and ROS-related spin-adduct signals were analyzed by electron paramagnetic resonance (EPR) spectroscopy. As shown in Figure 8, incubation with Mg-2Zn-0.2Ca-*x*Ag extracts resulted in higher ROS fluorescence intensity in both *E. coli* and *S. aureus*. The ROS fluorescence intensity showed an Ag-content-dependent increasing trend. Compared with the Ag-free alloy, the ROS fluorescence intensity of *E. coli* increased by approximately 1.38-, 1.64-, and 3.25-fold after exposure to extracts from alloys containing 0.1, 0.3, and 0.5 wt % Ag, respectively. Similarly, the ROS fluorescence intensity of *S. aureus* increased by approximately

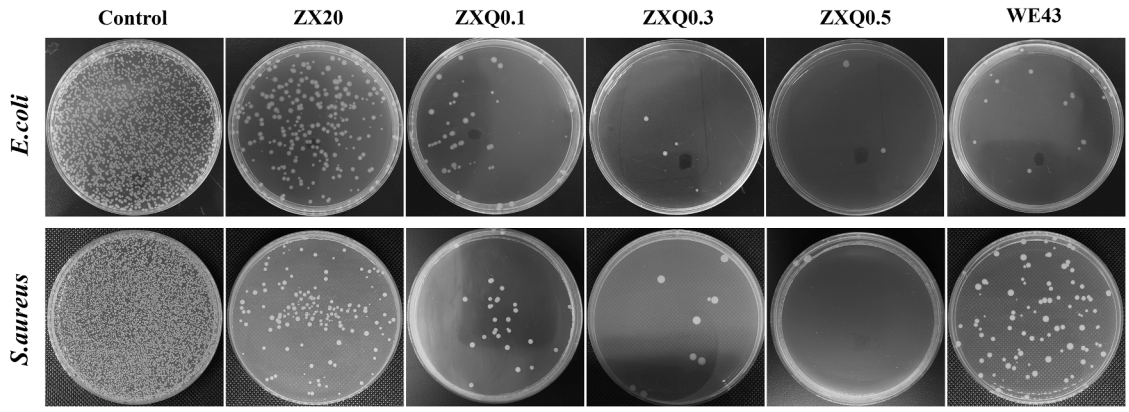


**Figure 4. Representative bacterial colonies of *E. coli* and *S. aureus* after 24 h of co-culture with extracts from as-extruded Mg-2Zn-0.2Ca-*x*Ag alloys**
Images are representative of three independent alloy extract preparations per group.

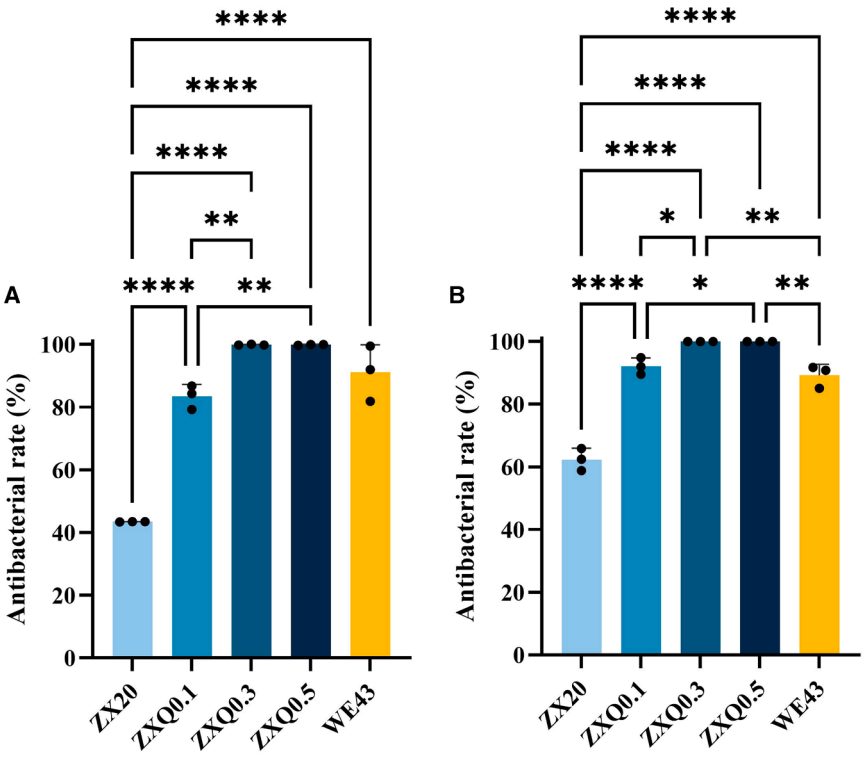


**Figure 5. Antibacterial rates of extracts from as-extruded Mg-2Zn-0.2Ca-*x*Ag alloys**

(A) Antibacterial rate against *E. coli*.

(B) Antibacterial rate against *S. aureus*.

Data are presented as mean ± SD ($n$ = 3 independent alloy extract preparations per group). $^{*}p < 0.05$, $^{**}p < 0.01$, $^{***}p < 0.001$, $^{****}p < 0.0001$.

0.71-, 0.82-, and 1.78-fold, showing a trend similar to the observed antibacterial response.

EPR spectra (Figure 9) further showed ROS-related spin-adduct signals assigned to hydroxyl radicals ($^{\cdot}OH$) and superoxide anion radicals ($O_2^{\cdot-}$) in the alloy extracts. Compared with the control, Mg alloy showed characteristic ROS-related spin-adduct signals. The $^{\cdot}OH$-related signal intensity was enhanced after Ag addition and increased with reaction time, particularly in the higher-Ag groups. Similarly, $O_2^{\cdot-}$-related spin-adduct signals were detected and were more evident in ZXQ0.5. These results suggest that Ag addition may promote ROS generation during Mg-2Zn-0.2Ca alloy degradation, providing supportive mechanistic evidence for oxidative-stress-mediated antibacterial activity.

## DISCUSSION

### Effect of Ag micro-alloying on the degradation behavior: Competition between corrosion product film regulation and micro-galvanic driving force

The degradation behavior of Mg-2Zn-0.2Ca-*x*Ag alloys is governed by the interplay between corrosion product film regulation and micro-galvanic driving forces associated with microstructural features. When exposed to physiological solutions, anodic dissolution of Mg leads to the formation of a $Mg(OH)_2$ corrosion product layer, which can temporarily increase interfacial resistance and retard corrosion propagation. However, in chloride-containing media, $Mg(OH)_2$ is unstable and converts to soluble $MgCl_2$, resulting in sustained $Mg^{2+}$ release and progressive alkalization.[34] The evolution of $Mg^{2+}$ concentration and pH observed in this study (Figures 1C and 1D) indicates a typical stage-dependent degradation behavior: an initial rapid degradation phase followed by a decelerated stage associated with corrosion product accumulation.

Low Ag addition (0.1 wt %) enhances corrosion resistance by stabilizing the protective corrosion product layer. At this content, Ag partially segregates into $Ca_2Mg_6Zn_3$ secondary phases along grain boundaries, slightly increasing their cathodic potential without strongly intensifying micro-galvanic coupling, allowing protective film formation to dominate degradation behavior, as evidenced by the relatively low corrosion current density and high polarization resistance observed for ZXQ0.1.[30,35] Consistently, ZXQ0.1 exhibited the lowest mass loss, degradation rate, $Mg^{2+}$ release, and pH elevation after 672 h of immersion in the present study (Figure 1). In contrast, higher Ag contents (0.3 and 0.5 wt %) increase Ag enrichment in the secondary phases, strengthen micro-galvanic coupling, and accelerate localized anodic dissolution.[12,27] These changes destabilize the corrosion product film and promote pit initiation and propagation, leading to deeper localized corrosion in SEM and 3D surface profiles (Figures S1 and S2). Together, these findings explain the non-linear degradation trend: minor Ag addition improves corrosion resistance, whereas higher Ag contents accelerate localized degradation.

From a biosafety perspective, $Mg^{2+}$ release from ZX20 and ZXQ0.1 remained within reported physiological ranges after long-term immersion, and *in vitro* pH elevations are expected to be buffered *in vivo*. Moreover, mildly alkaline environments have been reported to support osteogenesis and cell survival,[36,37] suggesting that low-Ag compositions may offer a potentially favorable degradation window while balancing degradation stability and functional performance. However, comprehensive evaluation of the biological performance of these alloys, particularly cytocompatibility, osteogenic responses, and related cellular mechanisms, is still required to establish their suitability for future biomedical applications.

### Antibacterial mechanisms: $Ag^{+}$-mediated ROS accumulation and alkalization synergistically drive antibacterial activity

The antibacterial activity of the Mg-2Zn-0.2Ca-*x*Ag alloys was primarily governed by two degradation-related factors: local alkalization, reflected by pH elevation during alloy degradation, and

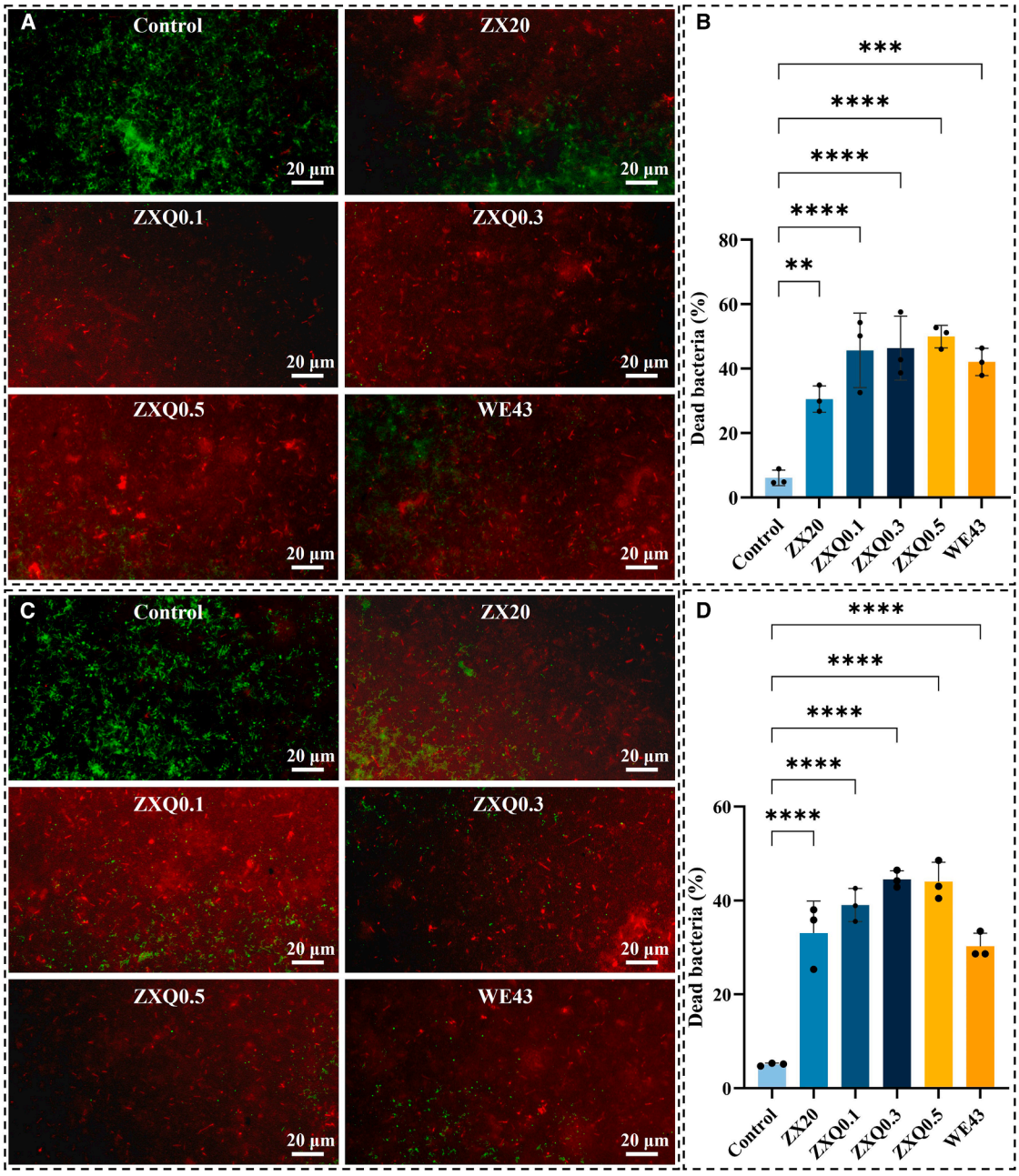


**Figure 6. Live/dead fluorescence staining of *E. coli* and *S. aureus* after 24 h of co-culture with extracts from as-extruded Mg-2Zn-0.2Ca-*x*Ag alloys**

(A) Representative fluorescence images of *E. coli* after co-culture with alloy extracts, showing live (green) and dead (red) cells. Scale bars: 20 μm.

(B) Quantitative analysis of dead *E. coli*.

(C) Representative fluorescence images of *S. aureus* after co-culture with alloy extracts, showing live (green) and dead (red) cells. Scale bars: 20 μm.

(D) Quantitative analysis of dead *S. aureus*.

Representative images were obtained from three independent alloy extract preparations per group. Data are presented as mean ± SD ($n = 3$ independent alloy extract preparations per group). $^{*}p < 0.05$, $^{**}p < 0.01$, $^{***}p < 0.001$, $^{****}p < 0.0001$.

increased metallic ion concentrations, particularly $Ag^{+}$. These factors collectively create an antibacterial interfacial microenvironment. The released $Ag^{+}$ ions and elevated pH may promote intracellular ROS generation (Figure 8) and inhibit ATP synthesis (Figure 7), leading to impaired bacterial adhesion (Figure 3) and viability (Figure 6). Recent studies support that Mg-based alloys exert antibacterial effects through degradation-mediated ion release, local alkalization, ROS-related oxidative stress, and

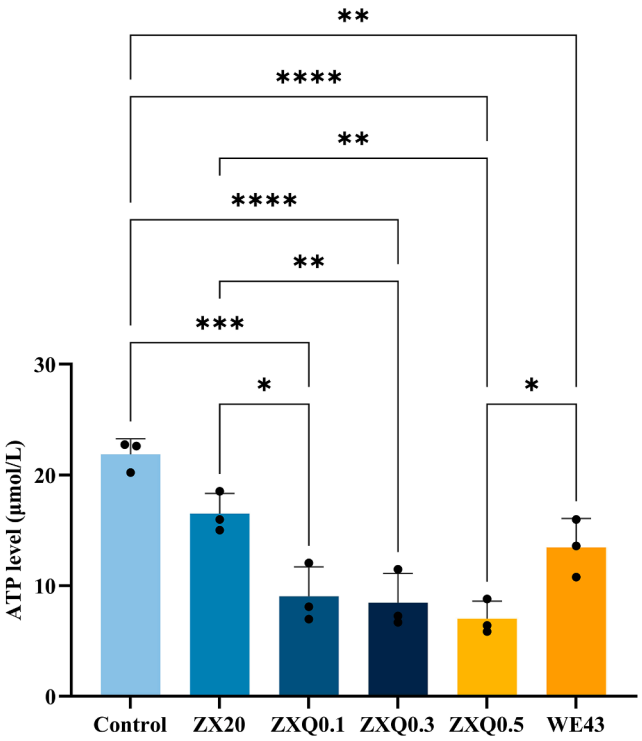


**Figure 7. ATP level of *E. coli* after co-culture with as-extruded Mg-2Zn-0.2Ca-*x*Ag alloys**

Data are presented as mean ± SD ($n = 3$ independent alloy extract preparations per group). *$p < 0.05$, **$p < 0.01$, ***$p < 0.001$, ****$p < 0.0001$.

interference with bacterial energy metabolism.[9,24,38] Corrosion-modified surfaces may further regulate bacterial adhesion through changes in surface morphology, roughness, and interfacial chemistry,[30,39] while $Ag^+$ release enhances membrane damage and metabolic disruption in Ag-containing alloys.[40]

The localized alkalization induced by Mg alloy degradation (pH > 9) is recognized as a key contributor to the inherent antibacterial properties of Mg-based materials.[41,42] Mechanistically, elevated $OH^-$concentrations alter the thermodynamic and kinetic conditions of redox reactions and directly disrupt bacterial metabolism. Proton extrusion during bacterial metabolism is neutralized by $OH^-$, collapsing the proton motive force across the cell membrane, which is essential for ATP synthesis. Consequently, ATP production is suppressed, impairing bacterial growth and viability. High pH also reduces bacterial surface hydrophobicity, further inhibiting adhesion to material surfaces.[40] In this study, ATP levels were markedly reduced in co-culture experiments (Figure 7), whereas Ag-containing alloys showed pronounced anti-adhesion effects (Figures 3 and S3), supporting the involvement of alkalization-mediated metabolic inhibition and adhesion suppression. Notably, WE43 extracts exhibited the highest pH but did not demonstrate the strongest antibacterial effect, indicating that alkalinity alone cannot account for the observed differences, and that metal ion contributions must be considered.

The role of $Mg^{2+}$ as a key antibacterial factor in Mg-based alloys remains controversial. Some studies report that high $Mg^{2+}$ concentrations inhibit bacterial adhesion and biofilm formation, yielding moderate antibacterial effects,[43,44] whereas other studies suggest that increasing $Mg^{2+}$ concentration alone does not necessarily enhance antibacterial performance, and that the antibacterial activity of pure Mg can be markedly weakened under neutral conditions.[45–47] In our study, WE43 extracts had the highest $Mg^{2+}$ concentration (Figure 2) but did not achieve maximal antibacterial efficacy, indicating that $Mg^{2+}$ was not the primary determinant of inter-group differences. By contrast, the Mg-2Zn-0.2Ca-*x*Ag alloys release $Zn^{2+}$ and $Ag^+$ during degradation, whereas WE43 lacks these ions. Both $Zn^{2+}$ and $Ag^+$ possess well-established antibacterial activity: electrostatic interactions with negatively charged bacterial membranes disrupt membrane integrity, impair nutrient uptake, and interfere with metabolism.[11,48] Importantly, both ions can induce ROS overproduction, leading to oxidative stress via lipid peroxidation, protein deactivation, and DNA damage, ultimately causing bacterial death.[49] Multi-metal ion interactions may

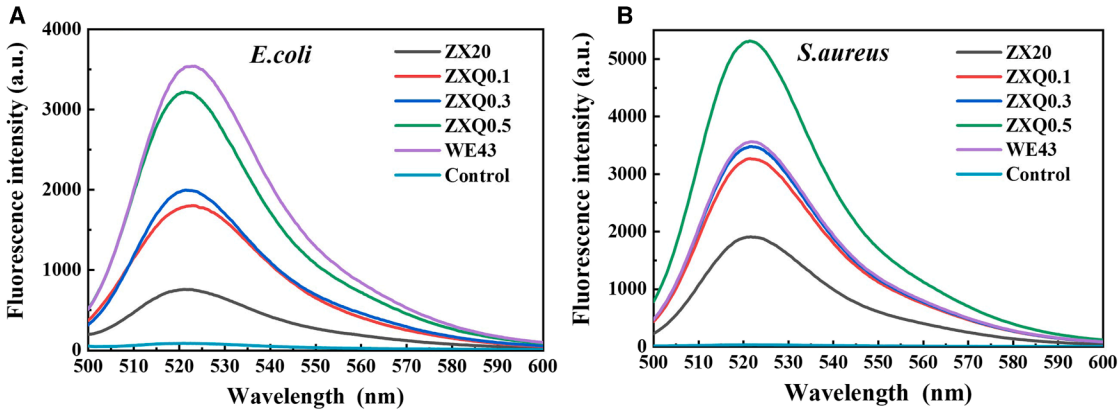


**Figure 8. ROS generation in bacteria after exposure to extracts from as-extruded Mg-2Zn-0.2Ca-*x*Ag alloys**

(A) ROS fluorescence spectra of *E. coli*.

(B) ROS fluorescence spectra of *S. aureus*.

Representative fluorescence spectra from one independent experiment are shown.

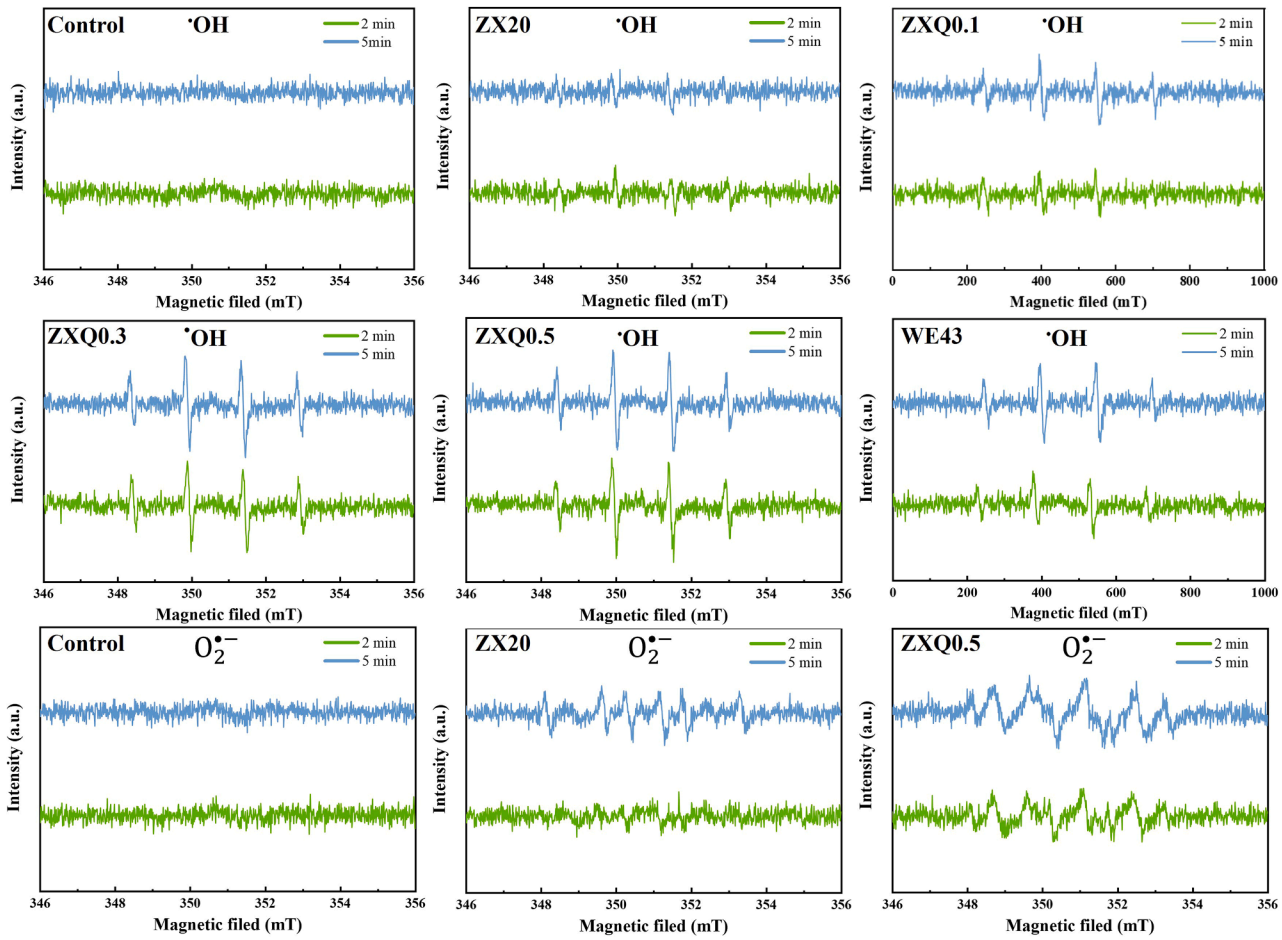


**Figure 9. EPR spectra of spin-adduct signals assigned to hydroxyl radicals and superoxide anion radicals in as-extruded alloy extracts at 2 min and 5 min**

Representative EPR spectra from one independent measurement are shown.

further enhance ROS generation through electron transfer processes, synergizing with proton gradient disruption and ATP depletion to amplify antibacterial effects.[11,50]

In this study, $Zn^{2+}$ concentrations were similar across different Ag-containing extracts, whereas $Ag^+$ levels increased significantly with Ag content, closely correlating with the observed gradient in antibacterial efficacy (Figures 2, 4, and 5). ROS-related measurements showed increased intracellular ROS, and EPR spectra showed stronger spin-adduct signals assigned to $^{\cdot}OH$ and $O_2^{\cdot-}$ (Figures 8 and 9), while ATP levels decreased correspondingly (Figure 7). These results collectively indicate that $Ag^+$ is the dominant tunable factor driving inter-group antibacterial differences, with $OH^-$ providing a basal inhibitory background, and $Ag^+$ (possibly with $Zn^{2+}$ synergy) amplifying bacterial killing via ROS induction and metabolic targeting.[48–50]

$Ag^+$ is a broad-spectrum antibacterial agent, exhibiting potent activity even at extremely low concentrations (0.1 ng/mL–0.1 μg/mL),[51] and is widely used in dental and orthopedic implant designs for infection prevention.[52–55] Ag-containing Mg alloys have been reported to release $Ag^+$ that contributes to bacterial cell disruption and death.[40] Its antibacterial mechanisms include penetration of the cell wall and membrane, binding to thiol (-SH) groups to disrupt membrane integrity and cause intracellular leakage, including ATP, inhibition of respiratory chain enzymes, interference with energy metabolism, and ROS-mediated damage to DNA, proteins, and lipids.[56] In this study, although Mg degradation-induced pH elevation provided a basal antibacterial background, the similar pH values of ZX20 and ZXQ0.1 extracts indicate that alkalization was not the main determinant of Ag-dependent antibacterial differences. Instead, the marked increase in $Ag^+$ concentration with Ag content suggests that $Ag^+$ release was the dominant composition-dependent factor. Correlation analysis further showed that antibacterial efficiency was positively associated with $Ag^+$ concentration and negatively associated with ATP level, supporting a quantitative association between antibacterial activity, $Ag^+$ release, and bacterial metabolic suppression (Figure S7).

ROS generation may arise from both alloy degradation-related reactions and bacterial intracellular oxidative stress. During Mg alloy degradation, anodic dissolution and cathodic reactions may promote dissolved oxygen reduction to $O_2^{\cdot-}$, which can further generate $H_2O_2$ and subsequently $^{\cdot}OH$ through

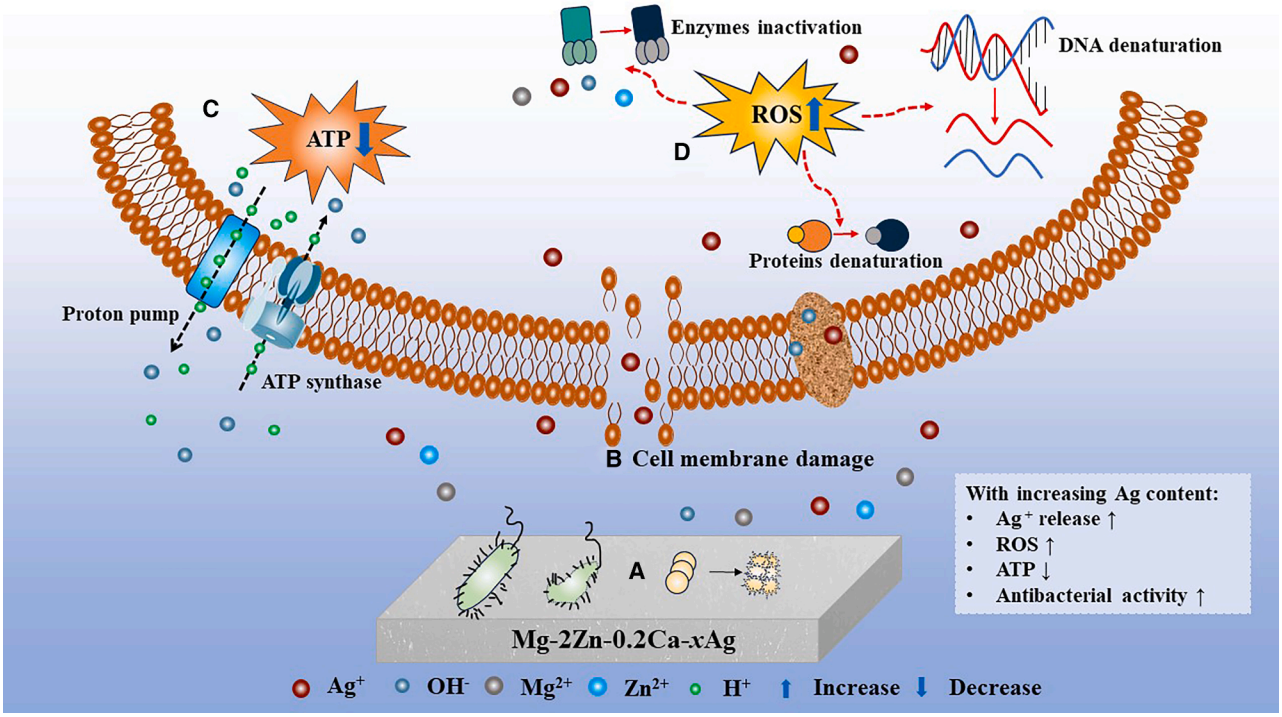


**Figure 10. Proposed antibacterial mechanism of as-extruded Mg-2Zn-0.2Ca-*x*Ag alloys**

(A) Contact killing.

(B) $Ag^+$-mediated disruption of bacterial membranes.

(C) ROS-induced damage to DNA, proteins, and the respiratory chain.

(D) $OH^-$-mediated neutralization of $H^+$ and inhibition of ATP synthesis.

metal-ion-mediated redox reactions.[57,58] In parallel, released antibacterial ions, particularly $Ag^+$, together with $Zn^{2+}$-associated changes in the local microenvironment, may disrupt bacterial membranes and interfere with respiratory electron transport, thereby inducing intracellular ROS accumulation.[59] Thus, the increased ROS levels (Figure 8) likely reflect the combined effects of alloy degradation, oxygen reduction, antibacterial ion release, and bacterial metabolic disruption. The observed trends in this study, namely ''increased $Ag^+$ release → enhanced ROS accumulation and reduced ATP levels → higher antibacterial activity of extracts,'' are consistent with the multi-target antibacterial mechanisms of $Ag^+$.[56] Furthermore, the sustained release of $OH^-$ and $Ag^+$ (with accompanying $Zn^{2+}$) during Mg-2Zn-0.2Ca-*x*Ag degradation, theoretically, may provide persistent antibacterial protection during the early high-risk phase of implantation, supporting its potential application in orthopedic infection prevention.

The antibacterial performance of Mg-2Zn-0.2Ca-*x*Ag alloys arises from the synergistic interplay between degradation-mediated $OH^-$ release and $Ag^+$ liberation. $OH^-$ disrupts bacterial proton gradients, inhibits ATP synthesis, and reduces adhesion, whereas $Ag^+$ exerts multi-target antibacterial effects, including membrane damage, metabolic suppression, and ROS generation.[49,50,55] Alloy extracts showed progressively enhanced antibacterial efficacy, increased ROS accumulation, and decreased ATP levels with increasing Ag content. Direct-contact assays further confirmed the inhibition of bacterial adhesion and growth. At 0.1 wt % Ag, enhanced corrosion resistance, controlled $Ag^+$ release, and moderate alkalization effectively suppressed bacterial activity; however, higher Ag contents (0.3 and 0.5 wt %) accelerated localized corrosion, amplified $Ag^+$ release and pH elevation, and intensified ROS-mediated ATP depletion, producing stronger antibacterial effects but compromising degradation stability. Collectively, these findings support a unified mechanistic framework of ''$OH^-$ basal inhibition + $Ag^+$-driven ROS/multi-target killing'' (Figure 10), highlighting low-Ag micro-alloying as an effective strategy to balance antibacterial potency with controlled degradation.

## Limitations of the study

Although the combination of degradation behavior analysis and multidimensional antibacterial metrics provides a robust mechanistic framework, extrapolation of the results to *in vivo* conditions requires caution because the present study was mainly conducted under static *in vitro* conditions. *In vitro* extract pH may reach 9–10; however, *in vivo* buffering, fluid exchange, protein adsorption, and tissue responses are likely to reduce both peak pH and residence time, and may also alter local ion concentrations, necessitating validation in dynamic and physiologically relevant models. Extract-based assays reflect the effects of diffusible factors, including $OH^-$ and released ions, whereas direct-contact assays highlight the

importance of the interfacial microenvironment in bacterial adhesion and biofilm formation, suggesting that local ion-release profiles may be key determinants of antibacterial performance. In addition, fluorescence-based ROS analysis was used as supportive mechanistic evidence. The observed Ag-content-dependent increase in ROS intensity, together with EPR spin-trapping signals, ATP depletion, live/dead staining, and SEM-observed membrane damage, supports the involvement of oxidative stress in the antibacterial mechanism. Considering the dose-dependent biological effects of $Ag^+$, future studies should comprehensively evaluate the cytocompatibility and biological performance of these alloys. In particular, investigations of osteoblast responses and osteogenic mechanisms will be important to elucidate their interactions with bone-related cells and validate their potential as biodegradable orthopedic biomaterials. Future studies should include replicated ROS quantification, characterize $Ag^+$ release kinetics, match antibacterial windows with cellular tolerance, combine antibacterial evaluation with cytocompatibility and osteogenic assessments, and integrate microelectrochemical mapping to correlate local corrosion features with interfacial antibacterial efficacy.

## RESOURCE AVAILABILITY

### Lead contact

Requests for further information and resources should be directed to and will be fulfilled by the lead contact, Yonghao Gao (gaoyonghao_009@163.com).

### Materials availability

This study did not generate any new, unique reagents, cell lines, or animal models.

### Data and code availability

- Data will be made available on request.
- No original code was generated in this study.
- Any additional information required to reanalyze the data reported in this paper is available from the lead contact upon request.

## ACKNOWLEDGMENTS

This research was supported by the Natural Science Foundation of Hunan Province-Joint Fund for the Medical and Health Sector, grant no. 2025JJ80899. D.G. appreciates the support from the UKRI MRC Future Leaders Fellowship (grant no. MR/T019123/2, UKRI1051) and NSFC (grant no. IEC\NSFC\211323).

## AUTHOR CONTRIBUTIONS

F.Y., conceptualization, methodology, investigation, data curation, formal analysis, writing – original draft, funding acquisition; Y.C., data curation, formal analysis, writing – review and editing; D.G., conceptualization, funding acquisition, writing – review and editing; L.Y., data curation, formal analysis, writing – review and editing; J.L., formal analysis, visualization, writing – review and editing; Y.G., conceptualization, supervision, methodology, validation, writing – review and editing. All authors have given approval to the final version of the manuscript.

## DECLARATION OF INTERESTS

The authors declare no competing interests.

## DECLARATION OF GENERATIVE AI AND AI-ASSISTED TECHNOLOGIES IN THE WRITING PROCESS

During the preparation of this work, the authors used no generative AI and AI-assisted technologies in the writing process and take full responsibility for the content of the publication.

## STAR★METHODS

Detailed methods are provided in the online version of this paper and include the following:

- KEY RESOURCES TABLE
- METHOD DETAILS
  - Preparation of alloys and extracts
  - Preparation of bacterial suspensions
  - *In vitro* degradation test
  - Bacterial adhesion morphology observation
  - Quantitative antibacterial assay
  - Bacterial live/dead staining
  - Intracellular adenosine triphosphate (ATP) quantification
  - Reactive oxygen species (ROS) detection
  - Electron paramagnetic resonance (EPR) spectral analysis
- QUANTIFICATION AND STATISTICAL ANALYSIS

## SUPPLEMENTAL INFORMATION

Supplemental information can be found online at https://doi.org/10.1016/j.isci.2026.117220.

Received: March 3, 2026
Revised: June 5, 2026
Accepted: July 28, 2026

## REFERENCES

1. Morgenstern, M., Kühl, R., Eckardt, H., Acklin, Y., Stanic, B., Garcia, M., Baumhoer, D., and Metsemakers, W.J. (2018). Diagnostic challenges and future perspectives in fracture-related infection. Injury *49*, S83–S90. https://doi.org/10.1016/s0020-1383(18)30310-3.
2. Arciola, C.R., Campoccia, D., and Montanaro, L. (2018). Implant infections: adhesion, biofilm formation and immune evasion. Nat. Rev. Microbiol. *16*, 397–409. https://doi.org/10.1038/s41579-018-0019-y.
3. Ghimire, A., and Song, J. (2021). Anti-periprosthetic infection strategies: From implant surface topographical engineering to smart drug-releasing coatings. ACS Appl. Mater. Interfaces *13*, 20921–20937. https://doi.org/10.1021/acsami.1c01389.
4. Malheiros, S.S., Borges, M.H.R., Rangel, E.C., Fortulan, C.A., da Cruz, N.C., Barao, V.A.R., and Nagay, B.E. (2025). Zinc-Doped Antibacterial Coating as a Single Approach to Unlock Multifunctional and Highly Resistant Titanium Implant Surfaces. ACS Appl. Mater. Interfaces *17*, 18022–18045. https://doi.org/10.1021/acsami.4c21875.
5. Marturano, V., Bizzarro, V., Ambrogi, V., Cutignano, A., Tommonaro, G., Abbamondi, G.R., Giamberini, M., Tylkowski, B., Carfagna, C., and Cerruti, P. (2019). Light-responsive nanocapsule-coated polymer films for antimicrobial active packaging. Polymers *11*, 68. https://doi.org/10.3390/polym11010068.
6. C, P.J., Rao, R.N., Golla, C.B., Özcan, M., and Prasad, P.S. (2025). Comprehensive review of Mg-based alloys: Mechanical, chemical and biological properties for prosthetic and orthopedic applications. J. Mater. Res. Technol. *35*, 2487–2502. https://doi.org/10.1016/j.jmrt.2025.01.215.
7. Tao, M., Cui, Y., Sun, S., Zhang, Y., Ge, J., Yin, W., Li, P., and Wang, Y. (2025). Versatile application of magnesium-related bone implants in the

treatment of bone defects. Mater. Today Bio *31*, 101635. https://doi.org/10.1016/j.mtbio.2025.101635.

8. Niu, E., Tong, J., Lu, H.B., Wang, S.W., Zhang, Q., She, J., and Chen, X. (2025). Controllable degradation behavior, mechanical properties and biocompatibility of Mg-Sr-Mn alloys for the orthopedic medical applications. npj Mater. Degrad. *9*, 113. https://doi.org/10.1038/s41529-025-00658-8.
9. Shahed, C.A., Ahmad, F., Günister, E., Foudzi, F.M., Ali, S., Malik, K., and Harun, W.S.W. (2023). Antibacterial mechanism with consequent cytotoxicity of different reinforcements in biodegradable magnesium and zinc alloys: A review. J. Magnes. Alloy. *11*, 3038–3058. https://doi.org/10.1016/j.jma.2023.08.018.
10. Wang, N., Ma, Y., Shi, H., Song, Y., Guo, S., and Yang, S. (2022). Mg-Zn- and Fe-Based Alloys With Antibacterial Properties as Orthopedic Implant Materials. Front. Bioeng. Biotechnol. *10*, 888084. https://doi.org/10.3389/fbioe.2022.888084.
11. Song, Q., Yang, L., Yi, F., Chen, C., Guo, J., Qi, Z., and Song, Y. (2024). Antibacterial Pure Magnesium and Magnesium Alloys for Biomedical Materials—A Review. Crystals *14*, 939. https://doi.org/10.3390/cryst14110939.
12. Wang, X., Huang, Y., Yang, L., Liu, Y., Wang, C., and Guo, E. (2024). Effects of Ga/Ag addition on corrosion behavior, cytotoxicity, and antibacterial activity of biodegradable Mg–2Zn alloy. J. Mater. Res. Technol. *29*, 3144–3155. https://doi.org/10.1016/j.jmrt.2024.02.060.
13. López, G.D., Williams, P.L., England, E., Wang, J., Boehlert, C., Llorca, J., and Echeverry-Rendón, M. (2025). Mg-Zn-Ca alloys for biodegradable medical implants. Part I: Effects of zinc and calcium on mechanical and corrosion behavior and cytocompatibility. Surf. Coat. Technol. *513*, 132519. https://doi.org/10.1016/j.surfcoat.2025.132519.
14. Jin, Y., Lyu, S., Yu, Q., and Chen, M. (2025). Optimizing the Mechanical Properties and Corrosion Performance of Low-Alloyed Mg-Zn-Ca Alloy by Regulating Zn/Ca Atomic Ratios. Solids *6*, 17. https://doi.org/10.3390/solids6020017.
15. Cho, D.H., Avey, T., Kwon, H., Dean, D., and Luo, A.A. (2025). A phase-based approach to optimizing the mechanical and corrosion properties of biodegradable Mg-Zn-Ca alloys. J. Alloys Compd. *1031*, 181127. https://doi.org/10.1016/j.jallcom.2025.181127.
16. Li, S., Li, H., Zhao, C., Wang, Z., Liu, K., and Du, W. (2022). Effects of Ca addition on microstructure, electrochemical behavior and magnesium-air battery performance of Mg-2Zn-*x*Ca alloys. J. Electroanal. Chem. *904*, 115944. https://doi.org/10.1016/j.jelechem.2021.115944.
17. Shan, Y., Qiao, B., Ouyang, S., Du, C., Zhao, L., Wang, G., Ye, J., Xiong, Y., Wei, Y., Song, J., et al. (2025). Biodegradable Mg-Ca/Mg-Cu bilayer membranes with enhanced mechanical, osteogenesis and antibacterial performances for GBR applications. J. Magnes. Alloy. *13*, 792–809. https://doi.org/10.1016/j.jma.2024.01.034.
18. Wang, C., Tang, S., Sun, Z., and Zhang, B. (2025). Effect of Cu content on microstructure and properties of biodegradable porous Mg-5Zn alloy scaffolds fabricated by SLM. J. Alloys Compd. *1049*, 185275. https://doi.org/10.1016/j.jallcom.2025.185275.
19. Liu, G., Han, J., Yu, X., Yuan, S., Nie, Z., Qiu, T., Yan, Z., Tan, C., and Guo, C. (2022). Influences of Extrusion and Silver Content on the Degradation of Mg-Ag Alloys In Vitro and In Vivo. Bioinorg. Chem. Appl. *2022*, 2557518. https://doi.org/10.1155/2022/2557518.
20. Zhang, X., Ba, Z., Wang, Z., He, X., Shen, C., and Wang, Q. (2013). Influence of silver addition on microstructure and corrosion behavior of Mg-Nd-Zn-Zr alloys for biomedical application. Mater. Lett. *100*, 188–191. https://doi.org/10.1016/j.matlet.2013.03.061.
21. Razzaghi, M., Kasiri-Asgarani, M., Bakhsheshi-Rad, H.R., and Ghayour, H. (2019). In Vitro Degradation, Antibacterial Activity and Cytotoxicity of Mg-3Zn-*x*Ag Nanocomposites Synthesized by Mechanical Alloying for Implant Applications. J. Mater. Eng. Perform. *28*, 1441–1455. https://doi.org/10.1007/s11665-019-03923-5.
22. Yu, L., Zhao, Z., Tang, C., Li, W., You, C., and Chen, M. (2020). The mechanical and corrosion resistance of Mg-Zn-Ca-Ag alloys: the influence of Ag content. J. Mater. Res. Technol. *9*, 10863–10875. https://doi.org/10.1016/j.jmrt.2020.07.088.
23. Khorasanian, M., Yeganeh, M., Gholamzadeh, N., and Alavi Zaree, S.R. (2021). Effect of Addition of Silver and Chilled Casting on Corrosion Behavior of AZ91 Magnesium Alloy. Int. J. Metalcast. *15*, 1184–1196. https://doi.org/10.1007/s40962-020-00558-4.
24. Chen, H., Yuan, B., Zhao, R., Yang, X., Xiao, Z., Aurora, A., Iulia, B.A., Zhu, X., Iulian, A.V., and Zhang, X. (2022). Evaluation on the corrosion resistance, antibacterial property and osteogenic activity of biodegradable Mg-Ca and Mg-Ca-Zn-Ag alloys. J. Magnes. Alloy. *10*, 3380–3396. https://doi.org/10.1016/j.jma.2021.05.013.
25. Ma, Y., Wang, D., Li, H., Yuan, F., Yang, C., and Zhang, J. (2020). Microstructure, mechanical and corrosion properties of novel quaternary biodegradable extruded Mg-1Zn-0.2Ca-*x*Ag alloys. Mater. Res. Express *7*, 015414. https://doi.org/10.1088/2053-1591/ab6a52.
26. Zhang, D.-D., and JIANG, S.-N. (2021). Effects of trace Ag on precipitation behavior and mechanical properties of extruded Mg-Gd-Y-Zr alloys. Trans. Nonferrous Met. Soc. China *31*, 3394–3404. https://doi.org/10.1016/S1003-6326(21)65737-0.
27. Asadollahi, M., Alizadeh, R., and Sadrnezhaad, S.K. (2023). Toward understanding the effects of solution heat treatment, Ag addition, and simultaneous Ag and Cu addition on the microstructure, mechanical properties, and corrosion behavior of the biodegradable Mg-2Zn alloy. J. Mater. Res. Technol. *26*, 1553–1571. https://doi.org/10.1016/j.jmrt.2023.07.258.
28. Yang, L., Shi, Y., Shen, L., Zhang, E., Qin, G., Lu, X., and Zhou, X. (2021). Effect of Ag on cathodic activation and corrosion behaviour of Mg-Mn-Ag alloys. Corros. Sci. *185*, 109408. https://doi.org/10.1016/j.corsci.2021.109408.
29. Bairagi, D., and Mandal, S. (2022). A comprehensive review on biocompatible Mg-based alloys as temporary orthopaedic implants: Current status, challenges, and future prospects. J. Magnes. Alloy. *10*, 627–669. https://doi.org/10.1016/j.jma.2021.09.005.
30. Yi, F., Cao, C., Chen, Y., Zeng, G., Gao, Y., and Liu, C. (2026). In-vitro corrosion and mechanical degradation of Mg-2Zn-0.2Ca-*x*Ag alloys in Hanks' solution. J. Alloys Compd. *1057*, 186770. https://doi.org/10.1016/j.jallcom.2026.186770.
31. Rosanoff, A., West, C., Elin, R.J., Micke, O., Baniasadi, S., Barbagallo, M., Campbell, E., Cheng, F.C., Costello, R.B., Gamboa-Gomez, C., et al. (2022). Recommendation on an updated standardization of serum magnesium reference ranges. Eur. J. Nutr. *61*, 3697–3706. https://doi.org/10.1007/s00394-022-02916-w.
32. Li, R., Chen, T., and Pan, X. (2021). Metal–Organic-Framework-Based Materials for Antimicrobial Applications. ACS Nano *15*, 3808–3848. https://doi.org/10.1021/acsnano.0c09617.
33. Zhang, X., Zhang, Z., Shu, Q., Xu, C., Zheng, Q., Guo, Z., Wang, C., Hao, Z., Liu, X., Wang, G., et al. (2021). Copper clusters: An effective antibacterial for eradicating multidrug-resistant bacterial infection in vitro and in vivo. Adv. Funct. Mater. *31*, 2008720. https://doi.org/10.1002/adfm.202008720.
34. Wang, Q., Liao, C., Liu, B., Jing, S., Guo, Z., Liang, L., Liu, J., Li, N., Zhou, R., Baker, I., and Wu, H. (2024). Enhanced corrosion resistance, antibacterial properties and osteogenesis by Cu ion optimized MgAl-layered double hydroxide on Mg alloy. J. Magnes. Alloy. *12*, 4174–4190. https://doi.org/10.1016/j.jma.2023.08.010.
35. Yin, J., Li, M., Yi, F., Zhao, X., Guan, D., Wang, K., Gao, Y., and Liu, C. (2024). Effects of micro-alloying Ag on microstructure, mechanical properties and corrosion behavior of extruded Mg-2Zn-0.2Ca-*x*Ag alloys. J. Alloys Compd. *989*, 174376. https://doi.org/10.1016/j.jallcom.2024.174376.
36. Zhang, J., Shen, X., Wang, Z., Yong, J., Jiang, Z., and Yang, G. (2025). Influences and strategies for bone regeneration based on microenvironment pH adjustment. Bone *196*, 117484. https://doi.org/10.1016/j.bone.2025.117484.

37. Wang, C.-X., Ma, T., Wang, M.-Y., Guo, H.-Z., Ge, X.-Y., Zhang, Y., and Lin, Y. (2021). Facile distribution of an alkaline microenvironment improves human bone marrow mesenchymal stem cell osteogenesis on a titanium surface through the ITG/FAK/ALP pathway. Int. J. Implant Dent. *7*, 56. https://doi.org/10.1186/s40729-021-00341-y.

38. Yang, N., Yang, X., Cheng, S., Gao, X., Sun, S., Huang, X., Ge, J., Han, Z., Huang, C., Wang, Y., et al. (2024). Magnesium implants with alternating magnetic field-enhanced hydrogen release and proton depletion for anti-infection treatment and tissue repair. Bioact. Mater. *38*, 374–383. https://doi.org/10.1016/j.bioactmat.2024.05.010.

39. Yuan, B., Chen, H., Zhao, R., Deng, X., Chen, G., Yang, X., Xiao, Z., Aurora, A., Iulia, B.A., Zhang, K., et al. (2022). Construction of a magnesium hydroxide/graphene oxide/hydroxyapatite composite coating on Mg-Ca-Zn-Ag alloy to inhibit bacterial infection and promote bone regeneration. Bioact. Mater. *18*, 354–367. https://doi.org/10.1016/j.bioactmat.2022.02.030.

40. Lin, Z., Sun, X., and Yang, H. (2021). The Role of Antibacterial Metallic Elements in Simultaneously Improving the Corrosion Resistance and Antibacterial Activity of Magnesium Alloys. Mater. Des. *198*, 109350. https://doi.org/10.1016/j.matdes.2020.109350.

41. Xie, J., Zhang, T., Jiang, J., Xue, W., Wang, W., Ni, J., Zhang, X., and Liu, X. (2025). Advances in magnesium-based implants for biomedical applications: A comprehensive review and future perspectives. J. Magnes. Alloy. *13*, 2978–3003. https://doi.org/10.1016/j.jma.2025.05.009.

42. Rahim, M.I., Eifler, R., Rais, B., and Mueller, P.P. (2015). Alkalization is responsible for antibacterial effects of corroding magnesium. J. Biomed. Mater. Res. A *103*, 3526–3532. https://doi.org/10.1002/jbm.a.35503.

43. Akbarzadeh, F.Z., Sarraf, M., Ghomi, E.R., Kumar, V.V., Salehi, M., Ramakrishna, S., and Bae, S. (2024). A state-of-the-art review on recent advances in the fabrication and characteristics of magnesium-based alloys in biomedical applications. J. Magnes. Alloy. *12*, 2569–2594. https://doi.org/10.1016/j.jma.2024.06.015.

44. Demishtein, K., Reifen, R., and Shemesh, M. (2019). Antimicrobial Properties of Magnesium Open Opportunities to Develop Healthier Food. Nutrients *11*, 2363. https://doi.org/10.3390/nu11102363.

45. Robinson, D.A., Griffith, R.W., Shechtman, D., Evans, R.B., and Conzemius, M.G. (2010). In vitro antibacterial properties of magnesium metal against Escherichia coli, Pseudomonas aeruginosa and Staphylococcus aureus. Acta Biomater. *6*, 1869–1877. https://doi.org/10.1016/j.actbio.2009.10.007.

46. Zhang, Y., Nie, T., Wu, Y., Gao, Z., Chen, D., Qian, K., Jiang, G., Liu, H., Shao, Y., Wang, C., et al. (2026). Recommendation for biological evaluations on biodegradable magnesium-based materials: Based on the coupling impact of pH value and $Mg^{2+}$ on cells and bacteria. J. Magnes. Alloy. *18*, 102015. https://doi.org/10.1016/j.jma.2026.102015.

47. Liu, C., Fu, X., Pan, H., Wan, P., Wang, L., Tan, L., Wang, K., Zhao, Y., Yang, K., and Chu, P.K. (2016). Biodegradable Mg-Cu alloys with enhanced osteogenesis, angiogenesis, and long-lasting antibacterial effects. Sci. Rep. *6*, 27374. https://doi.org/10.1038/srep27374.

48. Chen, K., Ge, W., Zhao, L., Kong, L., Yang, H., Zhang, X., Gu, X., Zhu, C., and Fan, Y. (2023). Endowing biodegradable Zinc implants with dual-function of antibacterial ability and osteogenic activity by micro-addition of Mg and Ag ($\leq$ 0.1 wt.%). Acta Biomater. *157*, 683–700. https://doi.org/10.1016/j.actbio.2022.12.012.

49. Damle, A., Sundaresan, R., Rajwade, J.M., Srivastava, P., and Naik, A. (2022). A concise review on implications of silver nanoparticles in bone tissue engineering. Biomater. Adv. *141*, 213099. https://doi.org/10.1016/j.bioadv.2022.213099.

50. Wang, X., Liu, S., Li, M., Yu, P., Chu, X., Li, L., Tan, G., Wang, Y., Chen, X., Zhang, Y., and Ning, C. (2016). The synergistic antibacterial activity and mechanism of multicomponent metal ions-containing aqueous solutions against Staphylococcus aureus. J. Inorg. Biochem. *163*, 214–220. https://doi.org/10.1016/j.jinorgbio.2016.07.019.

51. Campoccia, D., Montanaro, L., and Arciola, C.R. (2013). A review of the biomaterials technologies for infection-resistant surfaces. Biomaterials *34*, 8533–8554. https://doi.org/10.1016/j.biomaterials.2013.07.089.

52. Paiwand, S., Schäfer, S., Kopp, A., Beikler, T., Fiedler, I., Gosau, M., Fuest, S., and Smeets, R. (2025). Antibacterial potential of silver and zinc loaded plasma-electrolytic oxidation coatings for dental titanium implants. Int. J. Implant Dent. *11*, 12. https://doi.org/10.1186/s40729-025-00595-w.

53. Abdallah, O.M., Sedky, Y., and Shebl, H.R. (2024). Comprehensive evaluation of the antibacterial and antibiofilm activities of NiTi orthodontic wires coated with silver nanoparticles and nanocomposites: an in vitro study. BMC Oral Health *24*, 1345. https://doi.org/10.1186/s12903-024-05104-w.

54. Hawi, S., Goel, S., Caro, J., Bonet, R., Orrit-Prat, J., Endrino, J.L., Pearce, O., and Nishio, W. (2025). Antibacterial and osseointegration evaluation of silver ion-implanted orthopaedic implants. J. Micromanuf. *1–12*, 25165984251382378. https://doi.org/10.1177/25165984251382378.

55. Zhang, E., Zhao, X., Hu, J., Wang, R., Fu, S., and Qin, G. (2021). Antibacterial metals and alloys for potential biomedical implants. Bioact. Mater. *6*, 2569–2612. https://doi.org/10.1016/j.bioactmat.2021.01.030.

56. Xu, Z., Zhang, C., Wang, X., and Liu, D. (2021). Release Strategies of Silver Ions from Materials for Bacterial Killing. ACS Appl. Bio Mater. *4*, 3985–3999. https://doi.org/10.1021/acsabm.0c01485.

57. Kim, J., Gilbert, J.L., Lv, W.W., Du, P., and Pan, H. (2025). Reduction reactions dominate the interactions between Mg alloys and cells: Understanding the mechanisms. Bioact. Mater. *45*, 363–387. https://doi.org/10.1016/j.bioactmat.2024.11.020.

58. Kessler, A., Hedberg, J., Blomberg, E., and Odnevall, I. (2022). Reactive Oxygen Species Formed by Metal and Metal Oxide Nanoparticles in Physiological Media-A Review of Reactions of Importance to Nanotoxicity and Proposal for Categorization. Nanomaterials *12*, 1922. https://doi.org/10.3390/nano12111922.

59. Godoy-Gallardo, M., Eckhard, U., Delgado, L.M., de Roo Puente, Y.J.D., Hoyos-Nogués, M., Gil, F.J., and Perez, R.A. (2021). Antibacterial approaches in tissue engineering using metal ions and nanoparticles: From mechanisms to applications. Bioact. Mater. *6*, 4470–4490. https://doi.org/10.1016/j.bioactmat.2021.04.033.

60. Dapporto, M., Tavoni, M., Restivo, E., Carella, F., Bruni, G., Mercatali, L., Visai, L., Tampieri, A., Iafisco, M., and Sprio, S. (2022). Strontium-doped apatitic bone cements with tunable antibacterial and antibiofilm ability. Front. Bioeng. Biotechnol. *10*, 969641. https://doi.org/10.3389/fbioe.2022.969641.

61. Safavi, M.S., Khalil-Allafi, J., Restivo, E., Ghalandarzadeh, A., Hosseini, M., Dacarro, G., Malavasi, L., Milella, A., Listorti, A., and Visai, L. (2023). Enhanced in vitro immersion behavior and antibacterial activity of NiTi orthopedic biomaterial by HAp-Nb2O5 composite deposits. Sci. Rep. *13*, 16045. https://doi.org/10.1038/s41598-023-43393-3.

62. He, G., Wu, Y., Zhang, Y., Zhu, Y., Liu, Y., Li, N., Li, M., Zheng, G., He, B., Yin, Q., et al. (2015). Addition of Zn to the ternary Mg-Ca-Sr alloys significantly improves their antibacterial property. J. Mater. Chem. B *3*, 6676–6689. https://doi.org/10.1039/c5tb01319d.

63. Chen, H., Feng, B., Ren, Y., and Hao, J. (2024). Corrosion behavior of in-situ synthesized ZnO-containing coatings of AZ31B magnesium alloy by micro-arc oxidation in simulated body fluids. ChemistrySelect *9*, e202304605. https://doi.org/10.1002/slct.202304605.

## STAR★METHODS

### KEY RESOURCES TABLE

| REAGENT or RESOURCE | SOURCE | IDENTIFIER |
|---|---|---|
| Bacterial and virus strains | | |
| *Staphylococcus aureus* strain CMCC(B)26003 | Chinese National Center for Medical Culture Collections (CMCC), China | CMCC(B)26003 |
| *Escherichia coli* strain CMCC(B)44102 | Chinese National Center for Medical Culture Collections (CMCC), China | CMCC(B)44102 |
| Critical commercial assays | | |
| Calcein-AM/PI Live/Dead Cell Staining Kit | Solarbio, China | Cat#CA1630 |
| Enhanced ATP assay kit | Beyotime, China | Cat# S0027 |
| Reactive Oxygen Species (ROS) Detection Kit | Solarbio, China | Cat#CA1410 |
| Software and algorithms | | |
| GraphPad Prism | GraphPad Software | Version 8.0 |
| Image-Pro Plus image analysis software | Media Cybernetics, USA | Version 6.0 |
| Other | | |
| Mg-2Zn-0.2Ca-*x*Ag alloys | This paper | ZX20, ZXQ0.1, ZXQ0.3, ZXQ0.5 |
| Ti-6Al-4V alloy | Commercial supplier | N/A |
| WE43 alloy | Prepared in this study | WE43 |
| Inductively coupled plasma optical emission spectrometer (ICP-OES) | Spectro Analytical Instruments, Germany | SpectroBlue Sop |
| Inductively coupled plasma mass spectrometer (ICP-MS) | PerkinElmer, USA | NexION 2000 |
| Scanning electron microscope (SEM) | TESCAN AMBER, Czech Republic | AMBER |
| Electron paramagnetic resonance (EPR) spectrometer | Bruker BioSpin, Germany | EMXplus |

### METHOD DETAILS

#### Preparation of alloys and extracts

The preparation method for extruded Mg-2Zn-0.2Ca-*x*Ag alloys has been described previously.[30] Briefly, the alloys were fabricated by melting and direct-chill casting under an Ar protective atmosphere using high-purity Mg, Zn, Mg-25 wt. % Ca master alloy, and Ag billets as starting materials. The as-cast billets (Ø140 mm) were homogenized at 385°C for 20 h and subsequently hot-extruded into rods (Ø38 mm) under an extrusion ratio of 11:1 and a ram speed of 0.6 mm/s. The alloys were machined into 10 mm × 10 mm × 5 mm specimens for *in vitro* degradation test, 20 mm × 20 mm × 10 mm specimens for extraction, and discs with a diameter of 8 mm and a thickness of 2 mm for bacterial co-cultivation. The microstructure and mechanical properties of these alloys have been comprehensively reported in our previous study.[30] Ti-6Al-4V titanium alloy was used as the negative control due to its lack of intrinsic antibacterial activity, while WE43 served as the positive control as a clinically used biodegradable magnesium alloy with partial antibacterial properties. All samples were polished with SiC sandpaper (400#–3500#) and subjected to ultrasonic cleaning in absolute ethanol. After polishing, all alloy samples exhibited smooth metallic surfaces with no obvious morphological differences among groups before immersion.

Following ISO 10993-12, Mg-2Zn-0.2Ca-*x*Ag alloy samples were sterilized by low-temperature hydrogen peroxide plasma (LK/MJQ-100, Chengdu Laoken Medical Technology Co., Ltd., China) and immersed in Hank's solution (Biosharp, BL561A, China) at a surface area-to-volume ratio of 1.25 $cm^2$/mL for extraction at 37°C for 72 h. The supernatant was collected by centrifugation at 3000 rpm for 5 min and stored at 4°C. The pH values of the extracts were measured, and $Mg^{2+}$, and $Zn^{2+}$ concentrations were quantified using ICP-OES (SpectroBlue Sop, Spectro Analytical Instruments, Germany) after 30-fold dilution. The instrument was calibrated with standard solutions (0.1–5 mg/L), with a detection limit of approximately 0.01 mg/L. $Ag^+$ concentrations were measured using ICP-MS (NexION 2000, PerkinElmer, USA) after 6-fold dilution, with standard solutions (0.1–2.5 μg/L) and an approximate detection limit of 0.01 μg/L. All measurements were performed in triplicate.

### Preparation of bacterial suspensions

Gram-positive *Staphylococcus aureus* strain CMCC(B)26003 and Gram-negative *Escherichia coli* strain CMCC(B)44102, both obtained from Chinese National Center for Medical Culture Collections (CMCC), were used to evaluate the *in vitro* antibacterial performance of the alloys. In this study, the two bacterial strains were tested separately rather than as a mixed culture. This design was used to independently assess the antibacterial response of a representative Gram-positive and a representative Gram-negative bacterium, while avoiding potential confounding effects caused by interspecies competition, differential growth rates, or strain-specific susceptibility in mixed cultures. The bacterial concentration was adjusted according to a pre-established OD600-CFU/mL calibration relationship generated by serial dilution and colony counting. An OD600 of 0.08–0.10 corresponded to approximately $1 \times 10^8$ CFU/mL, followed by serial dilution to the required concentrations.[60–62]

### *In vitro* degradation test

Immersion tests were conducted in Hank's solution at 37°C to evaluate the *in vitro* degradation rates of the alloys. The immersion period lasted 672 h, with a solution-to-sample area ratio of 20 mL:1 $cm^2$ according to ASTM G31-72.[63] The pH was monitored during the test, and $Mg^{2+}$ concentrations were quantified using ICP-OES (Spectro Blue Sop, Germany) after 30-fold dilution. After 672 h, samples were acid-cleaned in a chromic acid solution ($CrO_3$, 200 g/L) for 10 min to remove corrosion products. The degradation rate (mm/y) was calculated using the formula:

$$P_w = \frac{K \times \Delta W}{A \times T \times D} \quad \text{(Equation 1)}$$

Where $K = 8.76 \times 10^4$ is a unit conversion constant, $\Delta W$ is the weight loss after immersion (g), $A$ is the exposed surface area with Hank's solution in $cm^2$, $T$ is the immersion time in h, and $D$ is the density of the sample in $g/cm^3$. Under these units, the calculated degradation rate is expressed as mm/y. This equation provides an average penetration rate and assumes uniform material loss over the exposed surface. Each experiment was performed in triplicate. To investigate the degradation morphology, SEM (TESCAN AMBER, Czech Republic) and laser scanning confocal microscope (Keyence VHKX200, Japan) were performed after corrosion products were removed following 3 h and 672 h of immersion.

### Bacterial adhesion morphology observation

The adhesion morphology of bacteria on the samples was observed using SEM (TESCAN AMBER, Czech Republic). A 1 mL suspension of bacteria ($1 \times 10^7$ CFU/mL) was co-cultured with each alloy sample for 4 h and 8 h. After incubation, the bacterial cells on the material surfaces were fixed with 2.5% glutaraldehyde and dehydrated through a graded series of ethanol solutions (20%, 40%, 60%, 80%, 100%), with each step lasting 5 min. Following dehydration, samples were freeze-dried and gold-coated for SEM observation. To evaluate the impact of alloy extracts on bacterial morphology, a 1 mL suspension of bacteria ($1 \times 10^7$ CFU/mL) was co-cultured with 4 mL of each alloy extract for 4 h, followed by collection and washing with PBS, and finally, the cells were plated on silicon wafers for SEM analysis.

For anti-adhesion assessment, each alloy sample was placed in a 24-well plate and completely submerged in 1 mL of *E. coli* and *S. aureus* suspensions ($1 \times 10^6$ CFU/mL), and incubated at 37°C for 24 h. After incubation, the samples were gently washed with sterile PBS to remove non-adherent bacteria. The samples were then transferred to centrifuge tubes containing PBS, and surface-adhered bacteria were eluted by ultrasound. The elution solution was diluted 10-fold serially, and 100 μL was spread on LB agar plates, incubated at 37°C for 18 h, and the colonies were counted. The anti-adhesion rate was calculated using the formula:

$$Anti - adhesion\ rate(\%) = \left(1 - \frac{N_x}{N_b}\right) \times 100\% \quad \text{(Equation 2)}$$

where ($N_x$) and ($N_b$) represent the number of colonies on the experimental group and titanium alloy control group, respectively. The experiment was repeated three times to ensure data reliability.

### Quantitative antibacterial assay

Alloy samples were placed in a 24-well plate and immersed in a suspension of bacteria ($1 \times 10^6$ CFU/mL) incubated at 37°C for 24 h. Subsequently, the culture was serially diluted 10-fold, and 100 μL of each dilution was evenly spread on LB agar plates and incubated for 18 h. The number of colonies was counted according to GB 4789.2–2016, selecting dilutions with colony counts between 30 and 300 CFU. The antibacterial rate (AR) was calculated using the formula:

$$Antibacterial\ rate(\%) = \left(1 - \frac{N_x}{N_b}\right) \times 100\% \quad \text{(Equation 3)}$$

where ($N_x$) and ($N_b$) represent the number of colonies on the experimental and control plates, respectively. The experiment was repeated three times to ensure data reliability. To further distinguish the effects of soluble degradation products from direct surface-contact effects, the antibacterial activity of the alloy extracts was assessed separately. A 100 μL ($1 \times 10^7$ CFU/mL) bacterial suspension was added to an microcentrifuge tube with 250 μL of alloy leachate and 650 μL of LB medium, with Hank's solution

replacing the leachate for the control group. After incubation at 37°C for 24 h, the same plating method was applied to calculate the antibacterial rate of the leachate.

### Bacterial live/dead staining

A total of 2.5 mL of each alloy leachate (LB medium for the control group) was mixed with 0.1 mL of bacterial suspension ($1 \times 10^8$ CFU/mL) and incubated at 37°C for 24 h. After incubation, the bacteria were collected by centrifugation, stained using the Calcein-AM/PI Live/Dead Cell Staining Kit (Solarbio, China) according to the manufacturer's instructions, and photographed using a fluorescence microscope. Live (green) and dead (red) cells were quantitatively analyzed using Image-Pro Plus 6.0 software (Media Cybernetics, USA).

### Intracellular adenosine triphosphate (ATP) quantification

Bacterial metabolic activity was assessed using an Enhanced ATP Assay Kit (Beyotime, China). Briefly, 1 mL of *E. coli* suspension ($1 \times 10^7$ CFU/mL) was incubated with each alloy sample at 37°C for 24 h. Bacteria in the culture system were collected and lysed according to the manufacturer's instructions. ATP levels were quantified via luminescence using a microplate reader. ATP concentrations were calculated based on a standard curve prepared with known ATP concentrations. A sterile glass slide was used as a blank control. The experiment was repeated three times to ensure data reliability.

### Reactive oxygen species (ROS) detection

To evaluate ROS generation induced by Mg-2Zn-0.2Ca-*x*Ag ($x = 0$, 0.1, 0.3, and 0.5 wt. %) and WE43 alloy extracts, intracellular ROS levels were detected using a 2′,7′-dichlorodihydrofluorescein diacetate (DCFH-DA) ROS assay kit (Solarbio, China) according to the manufacturer's instructions. Physiological saline served as a blank control. Bacterial suspension (1 mL, $1 \times 10^7$ CFU/mL) was incubated with 5 mL of each alloy leachate at 37°C for 24 h. After incubation, bacteria were collected by centrifugation and washed three times with PBS to remove debris. The DCFH-DA probe was added, and the mixture was incubated at 37°C in the dark for 30 min, with gentle mixing every 3–5 min to ensure uniform staining. After incubation, cells were washed three times with PBS to remove unbound probes. Fluorescence intensity was measured using a fluorescence spectrophotometer (Hitachi F-4500, Japan) at an excitation wavelength of 488 nm and an emission wavelength of 535 nm.

### Electron paramagnetic resonance (EPR) spectral analysis

ROS in the alloy extracts were further analyzed by EPR spectroscopy using 5,5-dimethyl-1-pyrroline N-oxide (DMPO) as the spin-trapping reagent. The alloy extracts were prepared in saturated NaCl solution to enhance spin-trapping detection of ROS under an accelerated chloride-rich degradation condition. Briefly, the test solution consisted of 20 μL of alloy extract and 30 μL of methanol, which was mixed with 50 μL of DMPO spin-trapping solution. The reaction mixture was immediately transferred into a quartz capillary tube for EPR measurement at room temperature using an EPR spectrometer (EMXplus, Bruker BioSpin, Germany). Spectra were collected at 2 min and 5 min after reaction, with the methanol solution without alloy extract serving as the control. The characteristic spin-adduct signals assigned to hydroxyl radicals ($^{\cdot}OH$) and superoxide anion radicals ($O_2^{\cdot-}$) were identified according to their typical EPR spectral patterns.

## QUANTIFICATION AND STATISTICAL ANALYSIS

Data are presented as mean values ± standard deviation (SD) from three independent replicates per group. Normality was assessed using the Shapiro-Wilk test. For normally distributed data, one-way ANOVA followed by Tukey's post hoc test was used for multiple group comparisons. For data that failed normality, the Kruskal-Wallis test followed by Dunn's multiple comparisons test was employed. To avoid potential bias associated with percentage-based antibacterial rates, especially near the upper limit of 100%, the colony-counting data were $\log_{10}$-transformed. Log-reduction values relative to controls were then used for normality assessment and statistical analysis, whereas antibacterial rates were retained for intuitive graphical presentation. Residual diagnostic analyses were performed to assess the assumptions of one-way ANOVA, including residual normality and homoscedasticity, and the corresponding results are provided in Figure S8. A $p$ value $<0.05$ was considered statistically significant. Statistical analyses were performed using GraphPad Prism version 8.0 (GraphPad Software, Inc., San Diego, CA, USA).